IEEE Transactions on Nuclear Science, Vol.NS-24, No.6, December 1977

AIR PRESSURE EFFECTS ON INTERNAL SGEMP: A BENCHMARK EXPERIMENT FOR COMPUTER CODE VALIDATION*

Raine M. Gilbert, Janis Klebers, and Alan Bromborsky+

Abstract

The effects of air ionization on the internal system-generated electromagnetic pulse have been examined parametrically in an electron-beam experiment performed as a benchmark for a computer-code validation program. A right circular cylinder containing a distribution of field and wall-current sensors was injected with a pulsed electron beam. Air pressure in the cylinder was varied between 1 mTorr and 3 Torr. Sensor responses are presented that show space-charge limiting of cavity current at the lowest pressures, space-charge barrier breakdown at intermediate pressures, and current pinch, current neutralization and the development of plasma tails at the higher pressures. Comparisons are made between representative measurements and the corresponding computer-code predictions.

I. Introduction

The internal system-generated electromagnetic pulse (internal SGEMP or IEMP) is an established threat mechanism for electronic systems exposed to the radiation environment of nuclear weapons. Ionization of residual air in the system cavities has been shown to have a strong effect on the SGEMP amplitude and waveshape. While this phenomenon has been understood qualitatively for several years, it has proven to be an extremely difficult effect to predict quantitatively, even with the help of high-speed computers. A benchmark experiment has been performed by Harry Diamond Laboratories (HDL) to provide a reliable data set for use in the Defense Nuclear Agency's (DNA) internal-SGEMP code-validation program. The experiment was designed to measure the effects of air pressure on the most important electron-transport phenomena affecting the generation of internal SGEMP; space-charge limiting, space-charge barrier breakdown, the development of plasma tails, current pinching, and current neutralization. Since no laboratory photon source existed that could provide the intense radiation flux required to study all of these effects in a single experiment, an electron beam generator (the SPI 6000) was used to inject the high-intensity electron driver directly. To open the validation program to the largest number of working SGEMP codes, of which many are two dimensional in r,Z cylindrical coordinates, an azimuthally symmetric geometry was selected for the experiment. Specifically, a right circular cylinder containing only field and current sensors was injected "end-on" with the electron pulse. The following material includes a description of the experiment, some representative results, and several comparisons between experimental measurements and corresponding computer code predictions.

II. The Experiment

A. Test Matrix: The objective of the experiment was to produce benchmark data for code validation; hence, it was important to produce high-confidence measurements using a variety of cavity depths, electron pulses, and air pressures. Practical considerations limited the test matrix to the following:

Pulse Lengths (ns, FWHM): 3, 13*
Cylinder Lengths (cm): 15, 30, 60
Air Pressures (Torr): 10^{-3}, 0.1, 0.3, 0.5, 0.7, 1.0, 1.5, 3.0+

* used only with 15 cm cylinder
\+ the highest air pressure producing no appreciable deformation of the Mylar membrane/wire mesh injection surface.

The cylinder diameter was fixed at 30 cm to match the electron beam diameter. Cavity length was varied with the addition or deletion of 5- and 10-cm-long cylinder. As will be shown later, the data obtained demonstrates virtually all of the phenomenology needed to meet the experimental objectives.

B. Test Configuration: Air pressure control in the test cavity was accomplished with a 1-m-long, 1-m-diameter vacuum tank fitted with specially made 95-ohm vacuum feed-through connectors.

The test volume itself was that bounded by the machine's exit mesh (4-mil tungsten) and the segmented cylinder shown in figure 1. Wall currents were measured with low-impedance resistor rings sandwiched between cylindrical segments and concentric sections of the end plate. In both

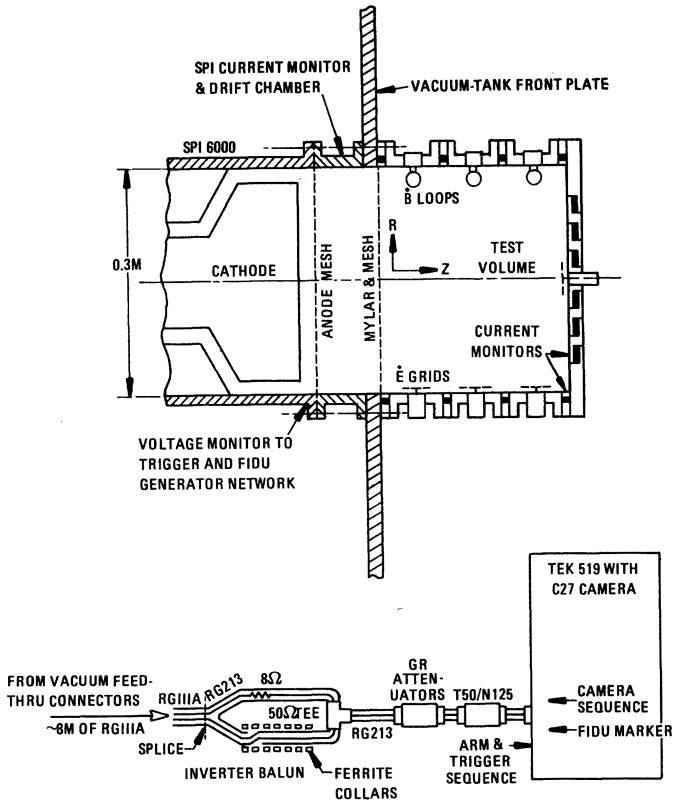

Figure 1. Experimental configuration: test cylinder (above) and inverter balun connection (below)

*This work was sponsored by the Defense Nuclear Agency under Subtask R99QAXEB089. Work unit title: "Internal EMP Generation and Interaction".

+Harry Diamond Laboratories, Department of the Army, 2800 Powder Mill Road, Adelphi, MD 20783

types of rings, resistor leads were virtually non-existent to minimize series inductance. All rings carried one-eighth-watt 3.3-ohm resistors, 360 of them in the largest rings, and 250, 165, and 80 in the three smaller concentric rings mounted in the end-plate assembly. Ring resistances were kept small so that the large wall currents, even those as high as several kiloamperes, would produce potentials too small to perturb primary electron trajectories or generate significant plasma current. Peripheral magnetic fields were measured with nine $\dot{B}$ sensors. Each was made of 50-ohm 0.085" semi-rigid cable and had a Möbius-loop geometry. Loop inductance was reduced by the insertion of a slotted copper cylinder having a 1.4-cm inner diameter and a 1.9-cm length. Sensor response time (L/R) was further shortened by placing a one-eighth-watt 100-ohm resistor in series with each pin in the loop's twinaxial connector.

The nine loops were distributed along the length of the cylinder in three sets of three, spaced 120 degrees between sensors. Six $\dot{E}$ grids were similarly distributed in two sets of three, with an additional circular $\dot{E}$ grid mounted axially on the central end-plate segment. Figure 1 shows the placement of the sensors. Each grid was a single-ended sensor; to minimize SGEMP noise pickup outside the test cylinder, the $\dot{E}$ signals were converted to the balanced state in a small inverter-balun placed just outside the cylinder wall. The balun was designed to accept the sensor signal on a 25-ohm coaxial lead, divide it in two on two parallel 50-ohm microstrip lines, invert the polarity of one branch signal with a Möbius connection and transmit the balanced result through an Amphenol twinaxial connector. Without exception, all sensor signals were transmitted to the oscilloscope rack on 95-ohm RG-111A balanced cables. There, inverter baluns converted each channel to the coaxial geometry required for input to the oscilloscopes. Two oscilloscopes were direct-accessed TEK 7904's and twenty-five were TEK 519's; all had a nominal 1-GHz bandwidth.

With this number of signal channels involved, it was necessary to field an automatic control system to synchronize the operation of the oscilloscopes and their cameras with the SPI 6000 electron pulse. This system consisted of two parts. One was a prebase sequencer built by Science Applications, Inc., from a synchronous motor set, for conditioning the recording equipment. It performed the following functions for all channels in a thirty-second sequence: 1) camera shutter open, 2) oscilloscope arm, 3) prebase trigger, 4) oscilloscope arm, and 5) camera shutter close.

The second part of the system was a network of pulse generators that provided thirty simultaneous fiducial time markers and 30 simultaneous sweep triggers for the oscilloscopes. Simultaneous is used here to mean $\pm$ 100 ps, a precision that was accomplished using avalanche transistors as follows: the SPI 6000 diode voltage monitor produced a voltage pulse that was used to initiate an impedance-matched cascade network of pulse generators. Each generator contained an avalanche transistor used as a gate for the discharge of a 50-ohm microstrip chargeline. The 30 fiducial generators each produced a 15-V pulse about 0.7-ns wide (FWHM); the 30 sweep-trigger generators each produced a 15-V pulse with a 20-ns width (FWHM) and rise and fall times comparable to those of the fiducial pulse. Cable lengths were chosen to insure that sweep triggers arrived at the oscilloscopes sufficiently in advance of fiducials and sensor signals to compensate for internal delays in the scope sweep circuits. The nominal timing sequence placed the fiducial mark one division into the 2 ns/division sweep, and the signal from the sensor one division after that. Fiducial pulses were inductively coupled into the signal line between signal attenuators and the oscilloscope. This arrangement insured a minimal influence on signal fidelity and provided a uniform fiducial amplitude throughout the experiment (nominally, a 1-mm amplitude as measured on the Polaroid film record).

C. Calibration of Equipment:

1. Sensor and Transmission Time: Care was taken during the calibration phase of the equipment to define the sensor response and the corresponding transmission-line transfer function over the full bandwidth of interest, 0 to 800 MHz. For this purpose, a 1.2-m-long, 0.3-m-diameter transmission-line calibrator was built to accomodate all of the test cylinder and sensors except the end-plate assembly. A 50-ohm ($\pm$ 2%) conical transmission-line segment brought the calibrator diameter from the input cable diameter to the diameter of the test cylinder, another reduced the calibrator diameter back to the cable size at the output. The 60-cm test cylinder, with all side-wall sensors in place, formed the outer conductor of the concentric transmission line; an equal length of aluminum pipe, 13.4 cm in diameter, formed the inner conductor.

The calibration pulse transmitted through the calibrator was a 250-V square pulse having a 0.5 ns, 10-to-90% rise time. This pulse was injected at 60-Hz repetition rate so that the sensor response, after transmission through its cable and balun, could be sampled with a time-sychronized Hewlett-Packard 1815B TDR/Sampler (the sampler bandwidth was in excess of 1 GHz). To insure that the transmission-line calibrator, sensors, and test cylinder produced no appreciable perturbation of the input calibration pulse, a direct comparison of input and output pulses was made using the same sampling procedure. The result showed a 1.5% reduction in transmitted amplitude and a barely discernible 1% increase in rise time.

The TEM field environment in the calibration volume and the transmitted responses were then Fourier analyzed. From these data, transfer functions in frequency space were derived for twenty-three channels, nine for $\dot{B}$ loops, eight for resistor-ring current monitors, and six for side-wall $\dot{E}$ grids. The three end-plate resistor rings and the one end-plate $\dot{E}$ grid were not calibrated; their responses have been left in raw data form. Notwithstanding the intention of unfolding the rest of the signal data using the appropriate transfer functions, a comparison of input signal and a mathematical integration of the raw output signal was made for a typical $\dot{B}$ loop. The integrated response showed good qualitative agreement with the calibration input signal. In general, the effects of unfolding the raw output were a sharpening of trace features and a 10 to 20% increase in signal amplitude.

When the sensors are operating in the electron-free environment of the transmission-line calibrator, the resulting data, unfolded with the correct

transfer functions, has a nominal accuracy of ± 10%, the bulk of the uncertainty being identified with digitization error in the data-unfold procedure. In the presence of dense electron clouds, the recessed resistor-ring sensors retain their ± 10% reliability, but the $\dot{B}$ loops are degraded to an estimated ± 20% because of imperfect common-mode rejection in the loop and localized nonuniformities in current density. The single-ended $\dot{E}$ grids are useful for factor-of-two accuracy only during their clear time, the time interval between the arrival of electromagnetic fields and the slower electrons that produced them. After this time, the $\dot{E}$ response is lost in the collected-current response of the grid. Apart from the innacuracies cited above, the integration of the $\dot{B}$ and $\dot{E}$ unfolded data can produce an error that is cumulative on the time axis; it is the baseline error introduced when the baseline for a time-derivative signal is digitized. It appears in the integrated result as an additive ramp of either positive or negative slope. The magnitude of this error at end-of-trace can easily be comparable to earlier signal peaks; in most cases, however, it can be identified and compensated for mathematically.

2. Oscilloscope Calibration The calibration of the oscilloscopes included a measurement of the horizontal sensitivity and a check on the uniformity of the vertical sensitivity across the face of the CRT. The vertical sensitivity was found by injecting a 120-V step function through calibrated attenuators, recording the trace on Polaroid film, and converting the trace deflection to a volts-per-film-millimeter ratio. The second part of the oscilloscope calibration was accomplished using a frequency-calibrated 1-GHz sine-wave generator. With the CRT beam swept at 2 ns/division, the sine-wave generator was connected to the vertical input, its amplitude raised sufficiently to cause a nominal ± ½-division deflection, and a film exposure taken. The sine-wave amplitude was then raised to a nominal ± 1 division and a double exposure of the film made. The resulting film record provided approximately 12 time-axis crossings at precise 1-ns intervals for sweep-speed calibration, and, in the distribution of approximately 48 sine-wave peaks, provided an area "map" of CRT vertical sensitivity. These calibration results were then incorporated in the conversion of film images to field and current magnitudes as functions of time.

D. Electron-Beam Characterization:

A complete characterization of the electron driver pulse would have required a measurement of injected current density as a function of time, position on the injection surface, electron energy, and polar angle relative to the injection-surface normal. This four-dimensional characterization matrix was beyond the capabilities of the available diagnostic equipment. Certain aspects of the SPI 6000 made this problem less severe. Since source electrons were accelerated across a common diode gap, their energies at the anode at a given time during the discharge were equal and their directions of travel were essentially parallel to the machine and test-cylinder axis. These conditions were smeared somewhat as the electrons passed through the two 0.1-mil mylar membranes between the anode mesh and the test volume; however, this spectral effect was observed to be severe only at the lower electron energies (20 keV). It was also established that careful adjustment of the machine electrodes could produce a ± 20% uniformity in injected current density over all of the injection surface except that annular area between r = 13 and r = 15 cm, where current density falls to 2/3 of nominal due to wall proximity effects.

Under these conditions, an adequate beam characterization was accomplished by (1) measuring the median injected electron energy as a function of time, (2) measuring the total injected current as a function of time,* and (3) establishing the time correlation between (1) and (2).

The energy of the electron at the emission side of the last Mylar membrane was measured with a focusing magnetic electron spectrometer. The spectrometer response time was determined using a time-domain reflectometer (TDR) having a multi-GHz bandwidth.

Each of the spectrometer's ten channels, when connected directly to the TDR, showed an e-fold response time of less than 0.25 ns; when the 3-m jumper cables used in the spectrometry were included in the TDR measurement, these responses increased to approximately 0.37 ns.

A shortage of TEK 7904's and 7A19 preamps (10 mV/div sensitivity and 500 MHz Bandwidth) precluded a one-shot record of the ten channel signals. Utilizing the strong shot-to-shot reproducibility displayed by the SPI 6000 electron-beam machine, a series of ten consecutive shots was used in each characterization to record the relative arrival time of each channel signal. Correlation of these arrival times was accomplished by choosing one channel for service as a fiducial time-mark designator, splitting its signal in two with a matched TEE, delaying one half of the signal a fixed amount to avoid overlap with other channel signals, and then duplexing this delayed reference with the channel signal in question. The electron-energy time dependence was then reconstructed using the electron-energy sensitivities of the spectrometer channels and the time intervals between the fiducial and the ten channel signals (including the one chosen for double duty as a time reference). The total injection current was measured with a low-impedance Faraday collector, which was a planar aluminum disc 20 cm in diameter placed 2 mm from the injection surface. The proximity of the collecting surface to the injection surface and the absence of significant air in the gap insured that the recorded signal reflected a current unperturbed by space-charge limiting, displacement current, or air-plasma effects.

The third experimental step in this characterization procedure was the time alignment of these two curves relative to each other. This was accomplished using the machine's diode voltage monitor as a common time reference during both current and energy measurements.

As a final part of the beam characterization, electron transport calculations were made on a computer to provide both energy and polar-angle dispersions as functions of the median electron energy at the emission side of the Mylar membrane.

*Note that when a portion of the injected current is space-charge limited, or $\dot{D}$ and/or plasma currents exist, this injected current is not the same quantity as total current at Z = 0.

The measurements of beam energy and injection current, as described above, were performed for the short and long pulses both before and after the short and long pulse parts of the IEMP experiment, respectively; no significant change in the performance of the SPI 6000 was observed during either phase. Figure 2 presents the results of the electron beam characterizations.

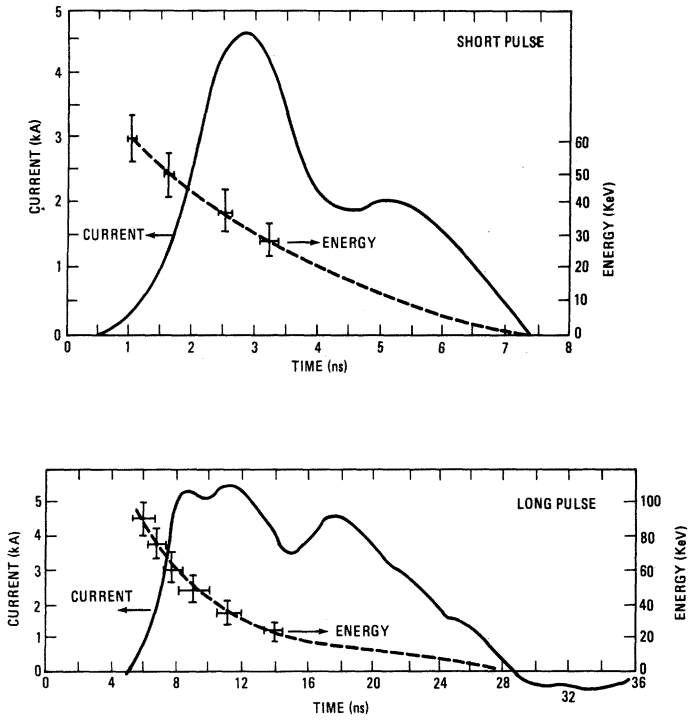

Figure 2. Electron beam characterizations: measured beam current and measured beam energy as functions of time for the short (3ns FWHM) and the long (13 ns FWHM) pulses

III. Experimental Results

The immediate objective of the experiment was the generation of benchmark data embracing the five phenomena that most strongly affect the development of internal SGEMP in air-filled cavities. The representative data contained in figures 3 and 4, which are the axial-current waveforms recorded during the long-pulse experiment at Z = 5 cm and Z = 15 cm, respectively, clearly show vacuum space-charge limiting after the initial injection of current (note that the baseline-to-baseline width of the long pulse is 24 ns), a partial space-charge barrier breakdown late in the pulse at 100 mTorr, a more complete barrier breakdown at 220 mTorr, the presence of a pronounced late-time plasma tail on the current pulse measured at 3.02 Torr, and finally, evidence of current neutralization at 3.02 Torr (current at this pressure peaks at a level below that obtained at 220 mTorr). The currents seen at Z = 5 cm are all twice as large as the corresponding currents seen at the rear of the cavity, Z = 15 cm. Except for this difference, the two sets of current traces are remarkably similar, both in waveshapes and relative amplitudes.* Thus, approximately half

* The polarity difference is a consequence of a cable-lead reversal at the Z = 15 cm sensor.

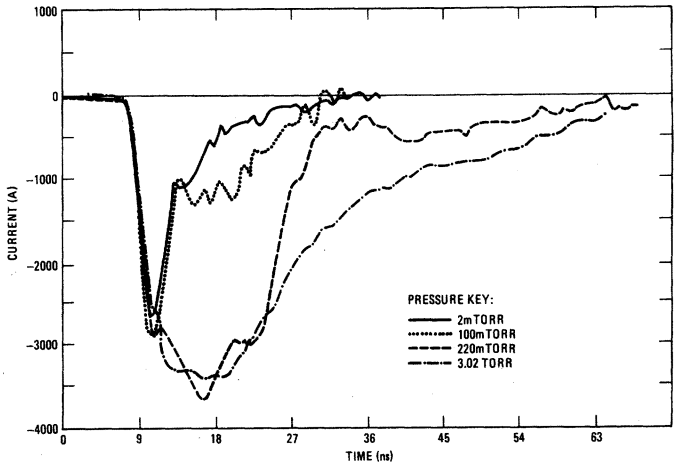

Figure 3. Long-pulse current measured in the resistor ring at Z=5cm for four air pressures

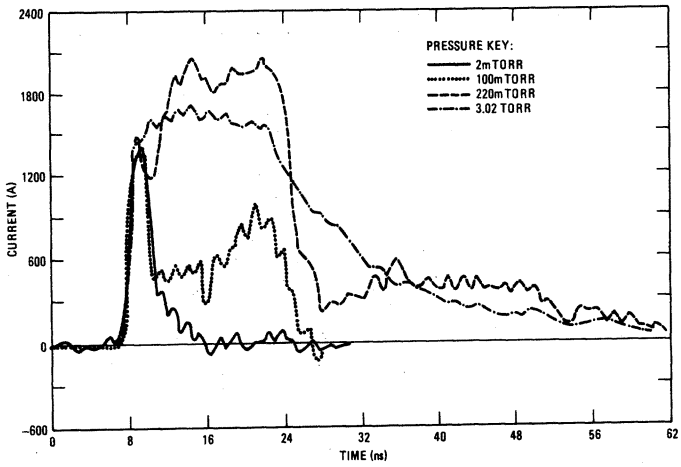

Figure 4. Long-pulse current measured in the resistor ring at Z=15cm for four air pressures

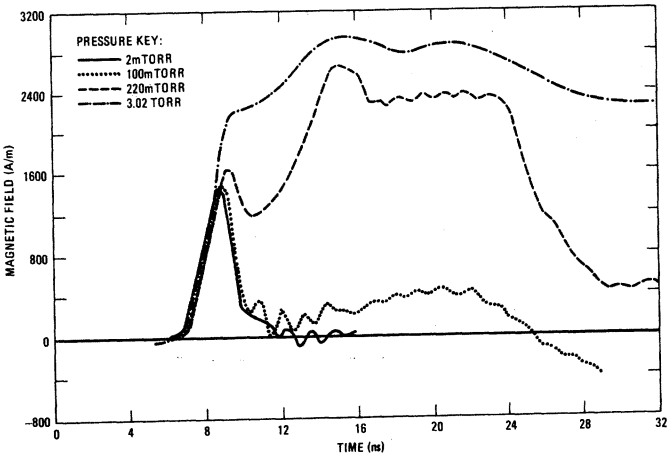

Figure 5. Long-pulse magnetic field measured at Z=12.5cm, r=13.8cm for four air pressures

of the current reaching Z = 5 cm and Z = 15 cm, irrespective of the air pressure. Figure 5 shows the magnetic field at r = 13.8 cm, Z = 12.5 cm, as reduced from time-derivative data produced by a $\dot{B}$ loop at those coordinates. Note that despite the appearance of base-line-error ramps in the 100 mTorr and 3.02-Torr traces, the qualitative agreement with current waveforms measured at Z = 15 cm is good. When the magnetic field magnitudes are converted to equivalent wall currents using 0.97 m

for the inside circumference of the cavity, and the location of the $\dot{B}$-loop (2.5 cm closer to the injection surface than the Z = 15 cm current sensor) is taken into account, it is seen that the qualitative agreement is joined by a convincing agreement in magnitudes.

Figures 6 and 7 give short-pulse data analogous to those given in figures 4 and 5 for the long-pulse experiment. Data for three air pressures are presented. Most of the observations made for the long-pulse results apply here, i.e., vacuum limiting after the initial injection of current is strong (the baseline-to-baseline width of the short pulse is 7 ns), a partial barrier breakdown occurs at 300 mTorr, a plasma tail extends measured current at 3 Torr well beyond the end of the injection pulse, and finally, the $\dot{B}$-loop and the current sensor agree with each other quite well. In the short-pulse data, there was no evidence of current neutralization, i.e., no reduction in net forward electron flux caused by plasma current directed backwards against injection current by the $\dot{B}$ electromotive forces in the cavity.

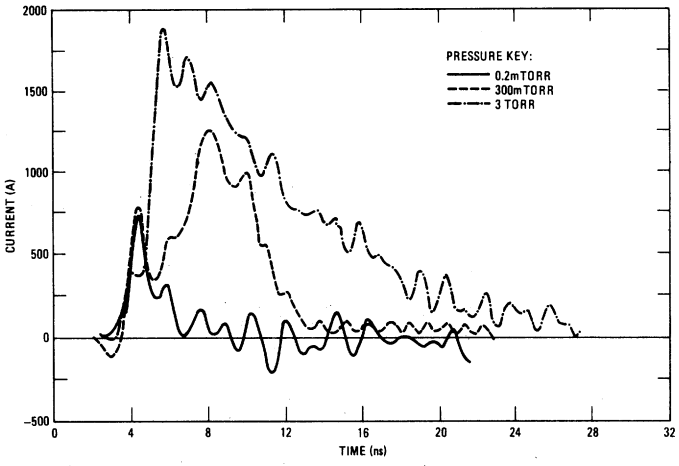

Figure 6. Short-pulse current measured in the resistor ring at Z=15cm for three air pressures

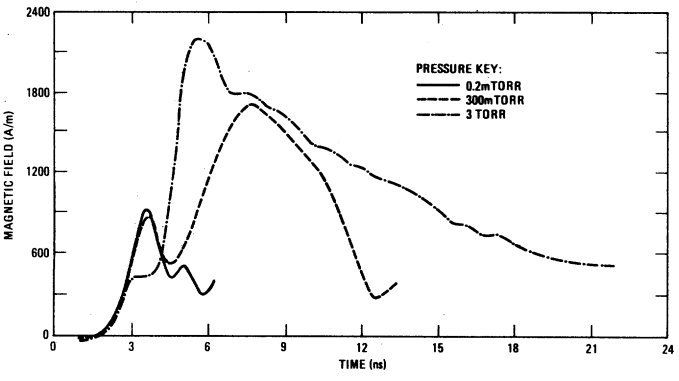

Figure 7. Short-pulse magnetic field measured at Z=12.5 cm, r=13.8 cm for three air pressures

Two other not unexpected differences in the long and short-pulse experiments were observed. The threshold for ionization-induced changes in the vacuum space-charge-limited waveform occurred at a lower air pressure for the long pulse than it did for the short pulse, specifically, between 50 and 100 mTorr for the long pulse, and between 200 and 300 mTorr for the short pulse.

The second difference is that all short-pulse waveforms, including those taken at 3 Torr, showed the amplitude dip after initial rise that is typical of space-charge limiting in the electron-beam environment. It should be pointed out that this particular limiting effect is largely a consequence of the rapidity with which electron energy drops after initiation of the diode discharge, even as injection current density is rising sharply. Like a light switch, limiting is "off" until the electron energy falls below the energy required to pass over the space-charge potential barrier, which, early in the pulse, is rising rapidly. When these two energy paths cross, limiting is initiated immediately; there is no gradual approach to a saturated value of transmitted current in the first half of the pulse that one might expect in the case of an electron flux characterized by a broad time-independent energy spectrum. Instead, transmitted current first follows the injected current, then drops sharply when limiting sets in. If air is present, ionization of air molecules will produce extra electrons that are responsive to the SGEMP fields, and an equal number of positive air ions that are relatively immobile. As the air electrons are driven to the walls by space-charge fields, they leave these positive ions behind. As the pulse continues, positive ions may accumulate in sufficient numbers to neutralize a significant part of the primary electron density, thereby reducing the associated space-charge fields. For a given primary electron pulse, the rate at which this barrier dissipation or breakdown progresses is determined by the density of air present. The short-pulse waveshapes show that the injection electron energy fell below the barrier-penetration level before the cumulative ionization density could reverse the growth of the space-charge barrier, even when the air pressure was as high as 3 Torr. The result: strong early-time limiting. In contrast, the long-pulse waveform for the transmitted current at 3.02 Torr shows no dip. Instead, it only pauses before resuming its rise, as if the trajectories of the electron energy and the barrier-penetration energy, both falling in time at this point, merged briefly before the barrier broke down completely. These particular characteristics of the electron-beam machine that make space-charge limiting so identifiable also increase the time separation between limiting and the onset of barrier breakdown, with the result that both can be examined in a single transmitted waveform (witness especially the current waveshapes in figure 4 for the intermediate air pressures).

The variation of peak transmitted current with distance along the cylinder axis is given for the four pressures of the long-pulse experiment in figure 8. At Z = 0 cm, measured peak transmitted current shows a much greater variation with air pressure than at Z = 5, 10, or 15 cm. In particular, at Z = 0, most of the transmitted-current increments associated with the increases in air pressure from 100 mTorr to 220 mTorr and from 220 mTorr to 3.02 Torr are lost to the side walls between Z = 0 and Z = 5 cm. A possible explanation for this can be

offered as follows: At vacuum and 100 mTorr, space-charge limiting insures that only the relatively energetic injected electrons contribute to the peak transmitted current; these are generally very forward directed and are least likely to be deflected by radial electric fields to the side walls before reaching the end of the cavity. At the higher pressures, the reduced space-charge barrier is a less effective discriminator, and passes those lower-energy electrons that are more responsive to residual radial electric fields. Moreover, figure 2 shows that at those times when the transmitted current peaks for 220 mTorr and 3.02 Torr, the energies of the injected electrons themselves are approximately 20 keV. Thus, even as these electrons reach the emission surface of the Mylar seal, they have been scattered over comparatively broad polar-angle distributions and are therefore more likely to be initially directed toward the side walls of the cylinder.

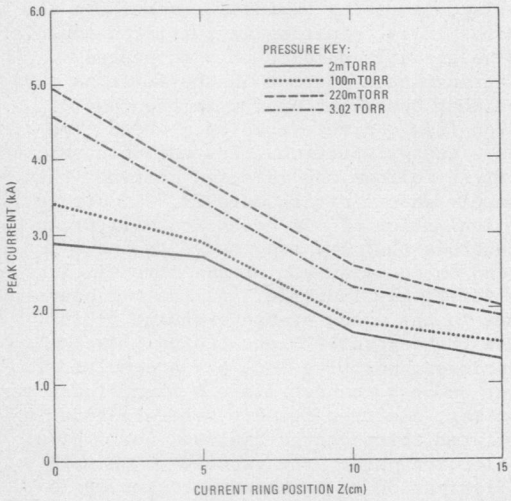

Figure 8. Long-pulse peak current variation along the axial direction measured at the current ring for four air pressures

The data discussed above has touched on four of the five phenomena sought in this experiment. The last, current pinching, occurs only when plasma conductivity neutralizes the electric fields that normally force a radial dispersion in an electron beam. When this dispersive effect is sufficiently weakened, the magnetic Lorentz force dominates and bends electron trajectories toward the beam axis, and a current pinch develops. Evidence of this effect occurred in the long-pulse experiment. Axial current density at Z = 15 cm is given in figure 9 as a function of distance from the cylinder axis for three of the four air pressures considered. (Current-densities for the fourth pressure were lost due to an isolated failure of the recording instrumentation serving the innermost end-plate current monitor). Current density profiles at vacuum and 100 mTorr suggest a "doughnut" distribution, while the profile for 3.02 Torr shows the highest current density lying on-axis, evidence of a pinched current. It must be noted here that this current-density data has been deduced directly from raw data. The impedances of the three end-plate current monitors have been scaled from the calibrated impedance of the 30-cm-diameter current sensor located at the same Z coordinate. The three scaling factors used were those based on resistor number ratios, since the three sensors had different numbers of nominally

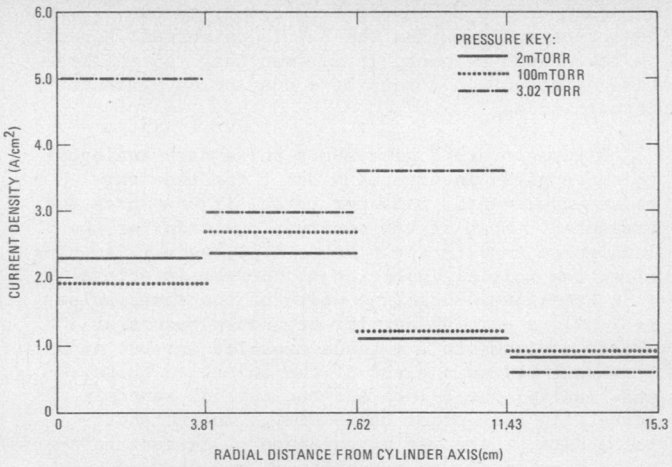

Figure 9. Radial distance from cylinder axis(cm) radial variation of current density at the cylinder end plate (Z=15cm) for three air pressures

identical 3.3- one-eighth-watt resistors. The plausibility of a current pinch at Z = 15 cm for 3.02 Torr is enhanced by the fact that, as discussed above, a significant current-neutralization effect was measured in the cavity at the same pressure. The two effects tend to go together, as both require a strong air-plasma conductivity.

During the short-pulse injections of the test cylinder, it became apparent that the cavity's TM_{010} resonant mode was not only strongly excited, but persisted long enough to allow measurement of ring-damping rates (see figure 10). This observation spurred an effort to translate the observed effects of air pressure on cavity resonance into an estimate of the cumulative ionization density at the end of the injection pulse. The details of this derivation are given in the appendix. In summary, the top trace in figure 10 shows a TM_{010}

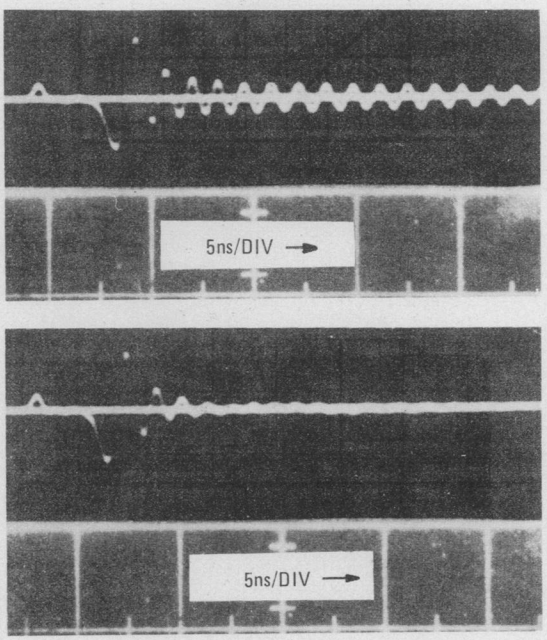

Figure 10. $\dot{B}$-loop response to short-pulse driver for air pressure equal to 2m torr (top) and 100m torr (bottom)

resonance at 690 MHz, 75 MHz less than the TM_{010} resonance for a perfect cylinder. (The presence of seven resistor-ring current sensors in series makes this difference reasonable.) The e-fold decay constant for the late-time ring was 8.84 ns. With 100 mTorr of air in the cavity, the resonance frequency shifted upwards to 742 MHz and the decay constant dropped to 2.80 ns. Relating these changes to the losses in the partially conducting air column gave an approximate value for the cumulative ionization density of 8×10^8 ion pairs/cm^3. Attention has been paid to this development because it may provide a means of measuring the very quantity that is most difficult to predict: the air-ionization density at those low pressures where fluid electron-transport treatments are inappropriate. At least it promises an approximate means of checking the accuracy of the computer code treatment of air ionization.

IV. A Preliminary Comparison of SGEMP Computer-Code Results with the Experimental Data

Two problems were formulated for the purpose of testing the capabilities of the existing SGEMP computer codes to predict the phenomena observed in the experiment. IEMP Problem II defined the experimental parameters for the short (3 ns FWHM) pulse, and IEMP Problem III defined the experimental parameters for the long (13 ns FWHM) pulse (Problem I was a purely hypothetical case, with no experimental data for comparison, and is not discussed in this report. Electron beam characterization shown in figure 2, plus ELTRAN predictions of electron dispersion in energy and polar angle for transmission through 0.2-mil Mylar (SPI 6000 mixing chamber conditions) were provided for Problems II and III. Quantities sought as the solution to both problems are listed below:

(1) Total current in the beam $I_T(t;Z)$ at Z = 0, 5, 10, and 15 cm. (t = time)

(2) Partial currents on end plate I(t;r) at Z = 15 cm for the limits r_o = 0 and 3.8, 7.6, 11.4, and 15.4 cm, where in terms of current net density J,

$I(t;r) = 2\pi \int_{r_o}^{r} J(t;r')\, r'dr'$ defines total current between r and r_o.

(3) $H_\phi(t;Z)$ at Z = 2.5, 7.5, and 12.5 cm; r = 13.8 cm

(4) E_Z at Z = 0 and Z = 15 cm; r = 0 cm

(5) E_r at Z = 2.5 cm and Z = 12.5 cm; r = 15.4 cm

All of the above were to be calculated at the following air pressures:

P = 0.2 mTorr, 300 mTorr, 3 Torr for Problem II, and

P = 2 mTorr, 100 mTorr, 220 mTorr, 3.02 Torr for Problem III.

Four independent SGEMP/IEMP code groups responded to Problems II and III prior to public release of benchmark data. The codes they used (herein identified as Codes A, B, C, and D) all employ finite-difference time-domain solutions of Maxwell's equations, and are fully-dynamic, self-consistent particle trackers. Special characteristics of the four codes are as follows: Codes A, B, and C are 2-dimensional in r,Z coordinates; Code A does not include avalanche multiplication of air ionization; Code B results have been supplemented with analytic calculations for conditions of high ionization density; Code D is 3-dimensional in cartesian coordinates, and employs a 3-species air-chemistry treatment.

Representative results are shown in figures 11, 12, and 13. Total current measured in the cylinder at Z = 15 cm is compared with the computer results at the respective air pressures designated for each problem in figures 11 and 12. Generally, a factor-of-two (or better) agreement in peak amplitude is observed between the measured and computed currents for the near-vacuum, and 3-Torr air-pressure conditions for both the long- and short-pulse cases. Qualitative waveshape comparison is also generally good [see figures 11(a), 11(d), 12(a), and 12(c)]. All of the code predictions, however, fail to show the $\dot{D}$ component of the current, which is most identifiable after the current pulse is over and the cavity mode oscillation continues.

The agreement between the measured and predicted results is relatively poor with respect to both peak amplitude and waveshape for the intermediate air pressures [see figures 11(b), 11(c), and 12(b)]. Not only do the code solutions depart significantly from the measurements, but they also vary widely among themselves in amplitude and waveshape, indicating a significant deficiency in the code models at intermediate air pressures.

Figure 13 shows a comparison of measured and computed peak current as a function of distance along the Z-axis of the cylinder for 2 mTorr and 220 mTorr (long pulse). Again, generally good agreement between the measured and computed results is apparent for the vacuum case (2 mTorr). Predicted results for 220 mTorr appear to bound the experimental data, but depart from the measurement to a greater extent.

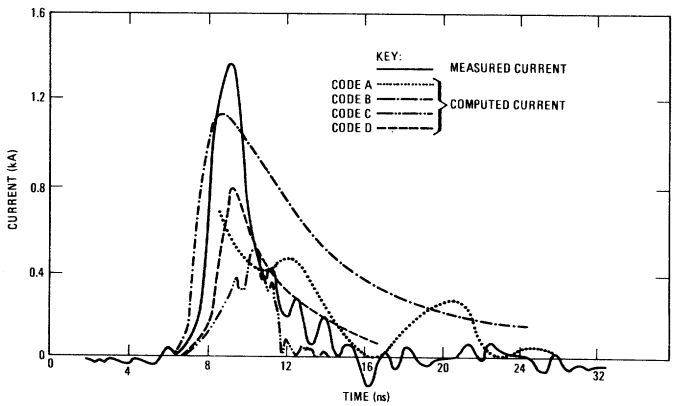

Figure 11a. Comparison of total current measured in the cylinder at Z=15cm with independent IEMP computer code predictions for an air pressure of 2m torr (long pulse)

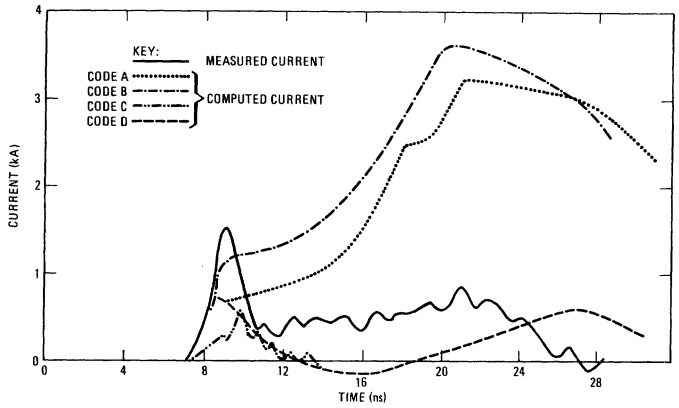

Figure 11b. Comparison of total current measured in the cylinder at Z=15cm with independent IEMP computer code predictions for an air pressure of 100m torr (long pulse)

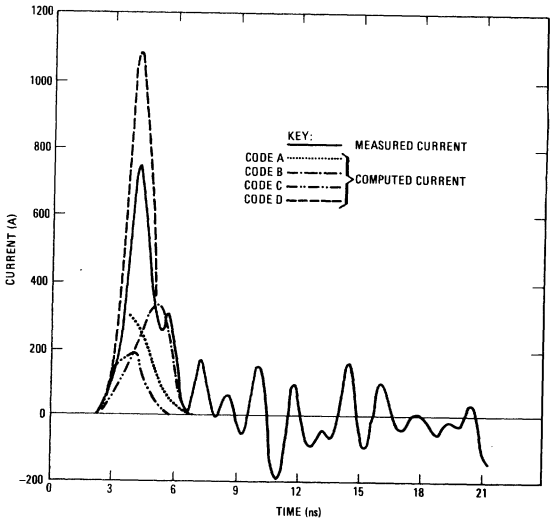

Figure 12a. Comparison of total current measured in the cylinder at Z=15cm with independent IEMP computer code predictions for an air pressure of 0.2m torr (short pulse)

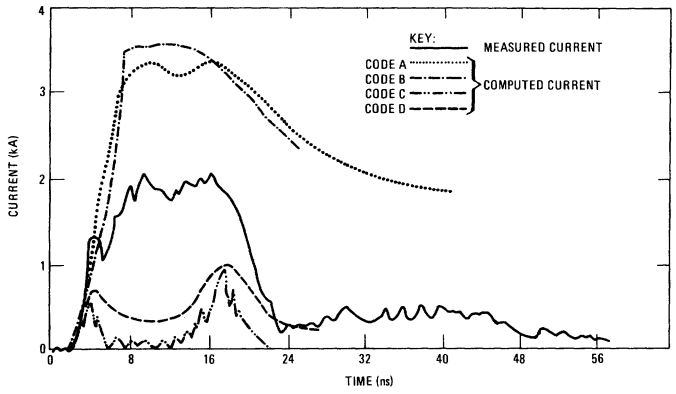

Figure 11c. Comparison of total current measured in the cylinder at Z=15cm with independent IEMP computer code predictions for an air pressure of 220m torr (long pulse)

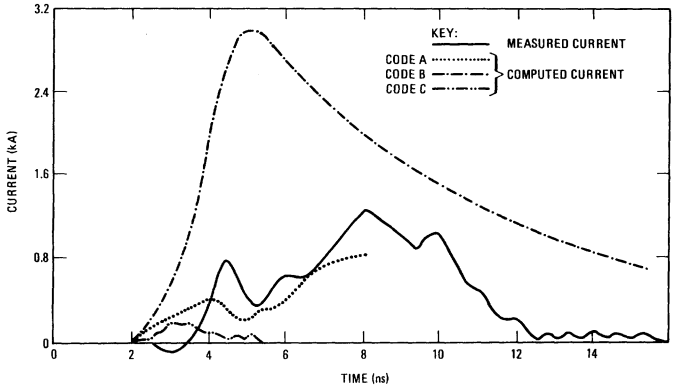

Figure 12b. Comparison of total current measured in the cylinder at Z=15cm with independent IEMP computer code predictions for an air pressure of 300m torr (short pulse)

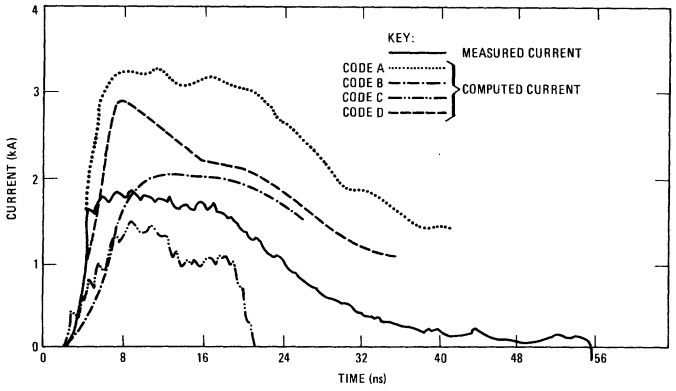

Figure 11d. Comparison of total current measured in the cylinder at Z=15cm with independent IEMP computer code predictions for an air pressure of 3.02 torr (long pulse)

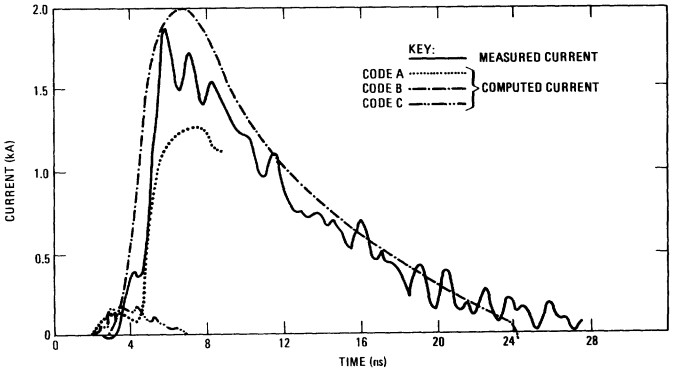

Figure 12c. Comparison of total current measured in the cylinder at Z=15cm with independent IEMP computer code predictions for an air pressure of 3 torr (short pulse)

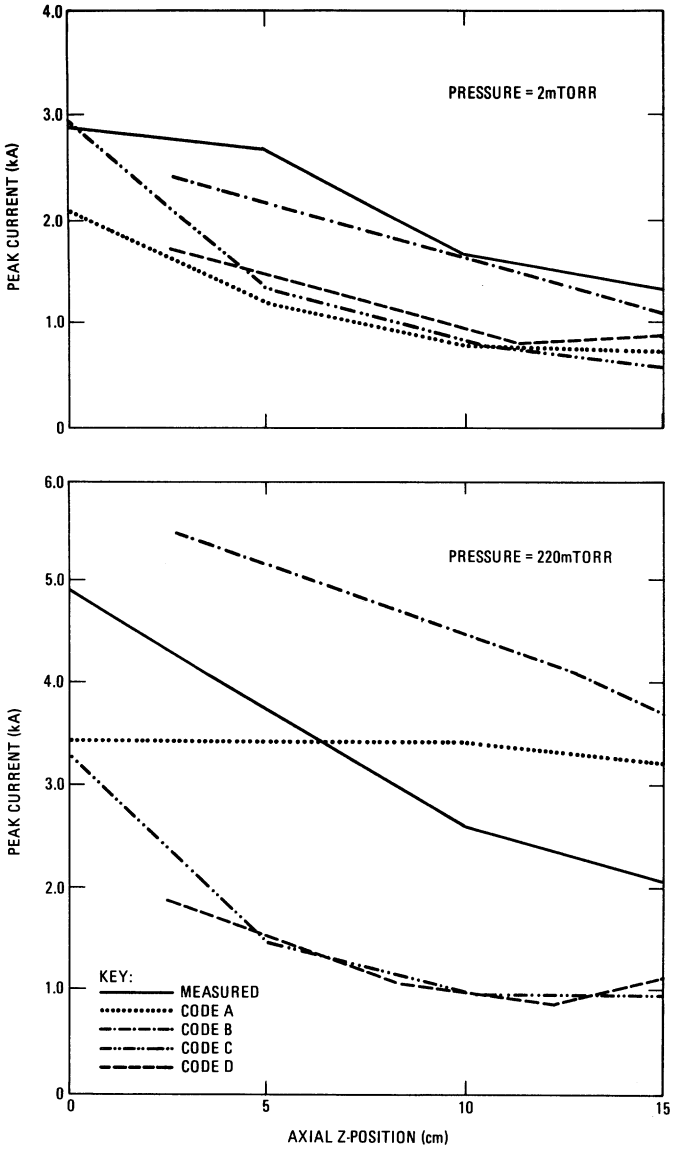

Figure 13. Comparison of measured and predicted peak current as a function of axial position for two air pressures (long pulse)

V. Conclusions

The experiment successfully produced benchmark data suitable for internal-SGEMP computer-code validation. Sensor design, sensor and instrumentation calibration, electron-beam characterization, and data reduction techniques all were directed towards maximizing data reliability. The two computer-code problems drawn from the test matrix showed that, for very low air pressure and pressures near 3 Torr in geometries having pronounced azimuthal symmetry, code predictions of currents and fields agreed with experiment in waveshape, and, in amplitude, to within a factor of two. At intermediate pressures measured in the hundreds of mTorr, however, code predictions departed radically from measured results, both quantitatively and qualitatively. Despite their common use of finite-difference solutions of Maxwells equations, the four codes even failed to agree with each other at these critical pressures. These observations suggest that improvements are needed in the various computer-code treatments of air-ionization for low pressures and high fields; this is the regime of avalanche ionization.

Acknowledgements

The authors wish to thank: Leroy Harper and Joe Schifano of Harry Diamond Laboratories, and Kenneth R. Sites of Science Applications, Inc., for major contributions to the experimental work; William D. Scharf and Phillip G. Dickerson for help in the report preparation, and the staff of Simulation Physics Inc., for their operation of the experimental facility and for their efforts in reducing the experimental data.

The authors would also like to acknowledge previous electron-beam experiments (references 3, 4, 5, and 6) which paralleled some aspects of the experiment reported here.

References

1. S. Ramo and J. R. Whinnery, Fields and Waves in Modern Radio, John Wiley and Sons, Inc., New York (1964), p. 425.

2. C. E. Baum, "Electron Thermalization and Mobility in Air," Electromagnetic Pulse Theoretical Notes, Air Force Weapons Laboratory, April 1971, Volume 1, Note 12, p. 12-11.

3. J. A. Rosado, "Space-Charge-Limited Currents in Cavities," DNA IEMP Symposium (U), DNA 3098P, June 1973 (SRD).

4. R. H. Stahl, et al., "Pressure Effects on Space-Charge-Limited Current Transmitted Across a Cylindrical Cavity," IEEE Trans Nucl. Sci. NS-20, No. 6, December 1973.

5. R. Fisher, et al., "Experimental SGEMP Results Using Electron-Beam Simulation," IEEE Trans. on Nucl. Sci. NS-22, No. 6, Dec. 1975, p.2392-96.

6. D. C. Osborn, R. H. Stahl, and T. N. Delmer, "Large-Area Electron-Beam Experiments on Space-Charge Neutralization in a Cavity," IEEE Trans on Nucl. Sci. NS-23, No. 6, December 1976.

APPENDIX

Air-ionization Effects on the TM_{010} Cavity Mode

The addition of partially ionized air at a pressure of 100 mTorr inside a resonant cylindrical cavity produces two effects on the cavity TM_{010}-mode oscillation which can be used to deduce the ionization density in the air. These effects are observed experimentally as an upward shift in the mode frequency, and as an increase in the mode damping rate. It is convenient to introduce the cavity Q factor for the computations:

$$Q \equiv \frac{\text{Energy stored in the mode}}{\text{Energy dissipated per mode cycle}} \equiv \frac{U}{u} \qquad (1)$$

If U is regarded as the stored energy time-averaged over half a cycle, then

$$U(t) = U_o\, e^{-\omega t/2\pi Q}, \qquad (2)$$

where U_o is some initial value of U.

The absolute magnitudes of the cavity fields and currents, also averaged over a half cycle, vary as $e^{-\omega t/4\pi Q} \equiv e^{-t/\tau}$, where τ is the field and current decay constant. Define Q_o and Q as the cavity Q parameters at vacuum and 100 mTorr, respectively; Q_d as the cavity Q the cylinder would have at 100 mTorr air pressure if there were no losses in the cylinder walls; ω_o and ω as the radian frequencies at vacuum and at 100 mTorr, respectively; u_o and u as the energies dissipated per cycle for resonances at vacuum and 100 mTorr, respectively; and u_d as the energy loss in the ionized air alone for resonance at 100 mTorr.

Assuming the difference in resonant frequencies for the two pressure conditions is small enough that skin depths in the aluminum cylinder wall are comparable, Q may be written as

$$Q = U/[u_o(\frac{\omega_o}{\omega}) + u_d] \qquad (3)$$

where the loss in the cylinder walls at vacuum resonance is scaled to the shorter period of the resonance at 100 mTorr. Rewrite Q from equations (1) and (3) in the following form:

$$Q = [\frac{1}{Q_o}(\frac{\omega_o}{\omega}) + \frac{1}{Q_d}]^{-1} \qquad (4)$$

and solve for Q_d:

$$Q_d = Q_o Q/[Q_o - (\frac{\omega_o}{\omega})Q] \qquad (5)$$

where $Q_o = \omega_o \tau_o/4\pi$, and $Q = \omega\tau/4\pi$.

From reference 1, Q_d may also be written as

$$Q_d = \frac{\omega\varepsilon}{\sigma}, \qquad (6)$$

where σ and ε are the conductivity and dielectric constant of the ionized air in the cavity. The dielectric constant ε may be found by attributing the observed frequency shift to the capacitive change in the series RLC analogue of TM_{010}-mode resonance. It was assumed earlier that the addition of air does not change cavity frequencies enough to alter skin depths significantly; this means that the resistance R and and the inductance L of the cavity have the same values both at vacuum and at 100 mTorr. Thus,

$$\frac{C}{C_o} = \frac{\varepsilon}{\varepsilon_o} = (\frac{\omega_o}{\omega})^2, \text{ or } \varepsilon = \varepsilon_o (\frac{\omega_o}{\omega})^2 \qquad (7)$$

The plasma conductivity can be written as $\sigma = ne\mu$, where n is the ionization density, e is the electron charge, and μ is the electron mobility. The mobility μ is given graphically as a function of $E(N_o/N)$ in reference 2, where E is the electric field and (N/N_o) is the fractional air density relative to standard.

The decay constants and resonant radian frequencies, as read from the $\dot{B}$-loop responses shown in Fig. 10, are $\tau_o = 8.84$ ns, $\tau = 2.80$ ns, $\omega_o = 4.34 \times 10^9 s^{-1}$, and $\omega = 4.66 \times 10^9 s^{-1}$. Using these values for τ and τ_o in equation (5), $Q_d = 1.29$. The frequency ratio, ω_o/ω, is 0.93. Hence, from equation (7), $\varepsilon = 0.865\ \varepsilon_o$, and $\sigma = \frac{\omega_o \varepsilon}{Q_d} = 0.028$ mho/m at 100 mTorr; the fractional air density relative to standard, (N/N_o), is 1.3×10^{-4}.

During TM_{010}-mode ringing, the longitudinal electric field E_Z and the azimuthal magnetic field H_ϕ are given by

$$E_Z = E_o J_o(k_o r) \qquad (8)$$

and

$$H_\phi = \frac{jE_o}{\eta} J_1(k_o r), \qquad (9)$$

where η is $(\mu/\varepsilon)^{\frac{1}{2}}$, r is the radial coordinate, and k_o is the wave number at TM_{010} mode resonance given by the lowest root of the boundary condition at the cylinder wall, $E_Z(R) = E_o J_o(kR) = 0$. At this wave number, $J_1(k_o R) = 0.52$ and equation (9) gives

$$E_Z(r=o) = 780\ H_\phi(r=R)$$

The $\dot{B}$ ring signal for r=R measured at 100 mTorr reflects an initial H_ϕ sinusoidal amplitude of approximately 100 A/m. Thus,

$$E_o = E_Z(r=0) = 7.8 \times 10^4 \text{ V/m}$$

A volume average of $E_Z(r) = E_o J_o(k_o r)$ over the range r=o to r=R is found using the identity

$$Z\, J_o(Z) = \frac{d}{dZ}\{ZJ_1(Z)\}. \qquad (10)$$

Then

$$\langle E_o \rangle_r = \frac{E_o}{\pi R^2} \int_o^R J_o(R_o r) 2\pi r dr = .43\ E_o$$

$$= 3.4 \times 10^4 \text{ V/m}.$$

The time average of $\langle E \rangle_r$ over one-half of a cycle gives $\langle\langle E_o \rangle_r \rangle_t = 2.2 \times 10^4$ V/m. A one-and-a-half decade extrapolation of the reference graph to the value of $E(N_o/N)$ found above gives an approximate electron mobility:

$$\mu \approx 230 \frac{m^2}{V \cdot s}$$

This extrapolation was necessary only because the ringdown signal used in this calculation was externally reduced by 26 db, the attenuation required for on-scale display of the largest signal peaks on the oscilloscope screen. Finally, using these values of conductivity and mobility,

$$n = \sigma/(e\mu) \approx 8 \times 10^{14} \frac{\text{ion-pairs}}{m^3} \qquad (11)$$

$$= 8 \times 10^8 \frac{\text{ion-pairs}}{cm^3}.$$